

# Impedance tuning with photoconductors to 40 GHz

 ISSN 1751-8768  
 Received on 10th August 2018  
 Revised 22nd October 2018  
 Accepted on 22nd January 2019  
 doi: 10.1049/iet-opt.2018.5102  
 www.ietdl.org

Jasper A. Drisko<sup>1</sup> ✉, Ari D. Feldman<sup>1</sup>, Franklyn Quinlan<sup>1</sup>, James C. Booth<sup>1</sup>, Nathan D. Orloff<sup>1</sup>, Christian J. Long<sup>1</sup>

<sup>1</sup>National Institute of Standards and Technology, 325 Broadway, Boulder, CO 80305, USA

✉ E-mail: jasper.drisko@nist.gov

**Abstract:** Light is widely used to control a variety of microwave devices, including switches, antennas, and detectors. Here, the authors present a photoconductive device integrated into a coplanar waveguide to tune complex impedances at microwave frequencies with applied light. The authors measured the current–voltage characteristics of the device as a function of the applied light intensity and fit the behavior to a known metal–semiconductor–metal junction model with two Schottky barriers. The authors also measured the frequency-dependent scattering parameters and extracted the device impedances in a Pi-network model. The devices showed three orders of magnitude impedance tunability from 100 MHz to 40 GHz, and the authors developed a circuit model to fit the frequency-dependent impedances. This simple device has applications in microwave electronics, microwave metrology, and multi-state calibrations.

## 1 Introduction

Photoconductive materials are widely utilised in microwave electronics as a part of select ultrafast switches [1, 2], antennas [3], waveform generators [4], detectors [5], photovaractors [6], and mixers [7, 8]. They offer a method of control beyond traditional transistor-based electronic circuits and logic, allowing for novel device architectures and functionality. Photoconductors are often employed due to their fast response times (on the order of picoseconds), which is essential for high-frequency modulation, tuning, and operation [9, 10]. Here, we propose a simple device to tune complex impedance at microwave frequencies with optical excitation.

The primary motivation for this work was to test whether or not photoconductors can exhibit a wide enough range of impedance states to serve as multi-state calibration artefacts for high-frequency (~1 MHz–100 GHz) measurements, similar to an approach discussed in a previously published algorithm [11]. Such a multi-state calibration artefact could reduce the time needed to perform a calibration by eliminating the need to make repeated connections to different calibration artefacts. The small size and simplicity of this device could also allow for calibration standards to be embedded in circuits or sensors where accurate measurements over the lifetime of the device are required. One key requirement for a multi-state calibration artefact is that it must be able to produce a variety of well-known impedance states over a wide frequency range. This differs from prior work on optically controlled microwave switches in that it requires more than simply ‘on’ or ‘off’ states. This current work contributes a new photoconductive device that enables a continuously tunable complex impedance with applied light. While our main target is multi-state calibration artefacts, tunable impedance is useful in a variety of applications, including but not limited to matching networks, filters, mixers, oscillators, switches, and variable loads.

## 2 Device design and experimental techniques

One major design consideration for microwave devices is compatibility with standard fabrication processes for integrated circuit technology. In this work, we demonstrate a simple, easy to fabricate, CMOS-compatible design for an optically tunable device. We used high-resistivity silicon as the photoconductive material, though other materials could provide different functionality, tuning regimes, or behaviour depending on the

application. For example, silicon has a bandgap of ~1.1 eV at room temperature and responds to excitation with the 980 nm wavelength laser we used in our experiments [12]. If one wanted to use a 1550 nm telecom wavelength to control the device, indium–gallium–arsenide (InGaAs), with a bandgap of ~0.75 eV, would be a suitable photoconductive material [13].

A schematic of the tunable impedance device is shown in Fig. 1a. The device was integrated into a coplanar waveguide (CPW) with a 50 µm gap in the centre conductor defining the active photoconductive region. Excited photocarriers conduct signals across the gap through the silicon. The tunable impedance devices were fabricated on standard 7.62 cm-diameter 20 kΩ cm ultra-high-resistivity silicon substrates to provide the maximum impedance tuning range. We spun a lift-off resist and photoresist onto the bare substrates, baked, and exposed with ultraviolet light using *i*-line stepper photolithography techniques. The resist was developed and the silicon's native oxide layer was removed with an inductively coupled plasma etch with fluorine chemistry. Then, 500 nm of gold was electron-beam evaporated onto the sample and a lift-off step was performed. The nominal dimensions of the CPWs were a 50 µm-wide centre conductor, 25 µm gap between the centre conductor and ground planes, and 200 µm-wide ground planes. A schematic of the fabrication process steps is shown in Fig. 2.

The tunable impedance devices were co-fabricated along with a set of on-wafer multi-line, thru, reflect, line (mTRL) standards for vector network analyser calibration [14]. A photograph of the measurement setup is shown in Fig. 1b. The mTRL standards were measured first and used to de-embed the photoconductive device measurements [14, 15]. We extracted the propagation constant from the mTRL calibration and used finite element simulations with the measured CPW dimensions to determine the distributed resistance per unit length ( $R$ ) and inductance per unit length ( $L$ ) as a function of frequency. We measured the gold conductivity to be  $(4.35 \pm 0.01) \times 10^7 \text{ S m}^{-1}$ , and used this value as an input in the finite element simulations. We then combined  $R$  and  $L$  from the simulations with the propagation constant to calculate the characteristic impedance of the CPW [16]. We used this characteristic impedance to impedance transform the mTRL error boxes from the characteristic impedance of the CPW to 50 Ω. We then used these error boxes in combination with a switch-term correction to obtain the error-corrected scattering parameter ( $S$ -parameter) measurements of the photoconductive devices. The on-

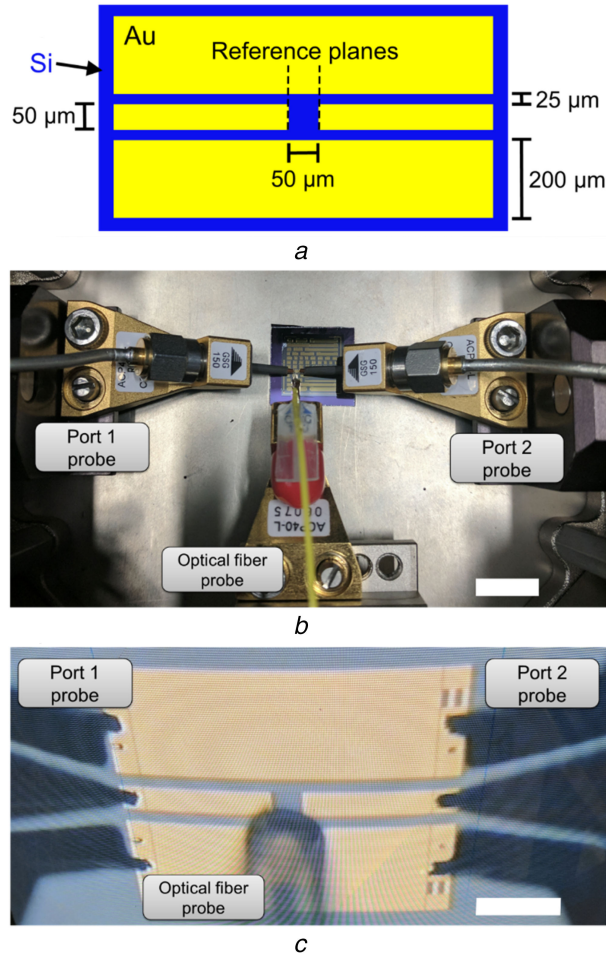


**Fig. 1** Device schematic and measurement setup

(a) Top-view schematic of the tunable photoconductive device embedded in a CPW, (b) Photograph of the measurement setup showing microwave and optical probes. Scale bar is 1 cm, (c) Photograph of the device integrated into the measurement setup. Scale bar is 200  $\mu\text{m}$

chip reference planes for the error boxes were at the edges of the gap in the gold centre conductor of the CPW (see Fig. 1a).

After performing the mTRL measurements, we positioned an optical fibre probe directly over the photoconductive region of the device (Fig. 1c). The optical fibre probe consisted of a cleaved, single-mode optical fibre (Corning HI 1060) connected to a 980 nm diode laser. Based on the nominal mode-field diameter (6  $\mu\text{m}$ ), beam divergence (140 mrad), probe angle ( $\pi/4$  rad), and probe-sample distance (300  $\mu\text{m}$ ), we estimate that the laser spot in the plane of the sample had a  $1/e^2$  diameter of  $\sim 50$   $\mu\text{m}$  along the axis of the CPW, and  $\sim 70$   $\mu\text{m}$  perpendicular to the axis of the CPW. Since a Gaussian beam integrated out to the  $1/e^2$  diameter contains  $\sim 86\%$  of the total power in the beam, and since the estimated  $1/e^2$  beam diameter is not occluded by any Au in the gap between the centre conductors, we expect at least 86% of the optical power from the probe to land in the gap between the two CPW centre conductors.

For each intensity of laser light we applied to the device, we measured both its direct-current (DC) current–voltage (I–V) characteristics and frequency-dependent  $S$ -parameters.

### 3 Results and discussion

The I–V characteristics of a representative device are shown in Fig. 3a. The conductivity was seen to increase with increasing laser intensity, which we attributed to generation of photoexcited carriers. The symmetric I–V curves are similar to other data from MSM junctions that have been previously studied [17–19]. Elhadidy *et al.* provide a theoretical model for such a junction. At

low bias, the junction current is dominated by the reverse biased Schottky contact and is given by [17]

$$I = A_2 A^* T^2 \exp\left(-\frac{q\phi_b}{kT}\right) \exp\left(\frac{q}{kT} \left(\frac{q^3 N_A}{8\pi\epsilon^3}\right)^{1/4} \left(V_i + V - \frac{kT}{q}\right)^{1/4}\right) \quad (1)$$

where  $A_2$  is the contact area,  $A^*$  is the Richardson constant,  $T$  is the temperature in Kelvin,  $\phi_b$  is the potential barrier height at zero bias,  $k$  is Boltzmann's constant,  $q$  is the electron charge,  $N_A$  is the density of available carriers,  $\epsilon = \epsilon_0 \epsilon_r$  is the semiconductor permittivity,  $V_i$  is the diffusion potential, and  $V$  is the applied bias. We found good agreement between this model and our data (solid lines in Fig. 3a). To obtain the fits, we took  $A_2 A^* = 9.5 \times 10^{-4}$  A K $^{-2}$ ,  $T = 300$  K,  $V_i = 0.1$  V, and  $\epsilon_r = 11.7$  to be exact values, lumping all the fit uncertainty into  $N_A$ . The fit values of  $N_A$  vs. laser intensity are shown in Fig. 3b.  $N_A$  increased sharply below 250 mW applied laser power and tended to saturate above 500 mW. We attributed the sharp increase in carrier density at low laser powers to photoexcited carriers and the saturation at high laser powers to an increased carrier recombination rate at high carrier densities.

As one moves from DC measurements to high-frequency measurements, the circuit analysis is complicated by parasitic capacitances and inductances in addition to resistances. To characterise these effects, we performed  $S$ -parameters measurements of a photoexcited device (Fig. 4). The  $S$ -parameters were highly tunable by varying the applied laser intensity, changing by several orders of magnitude over the full frequency range investigated. This large variability is desirable for a multi-

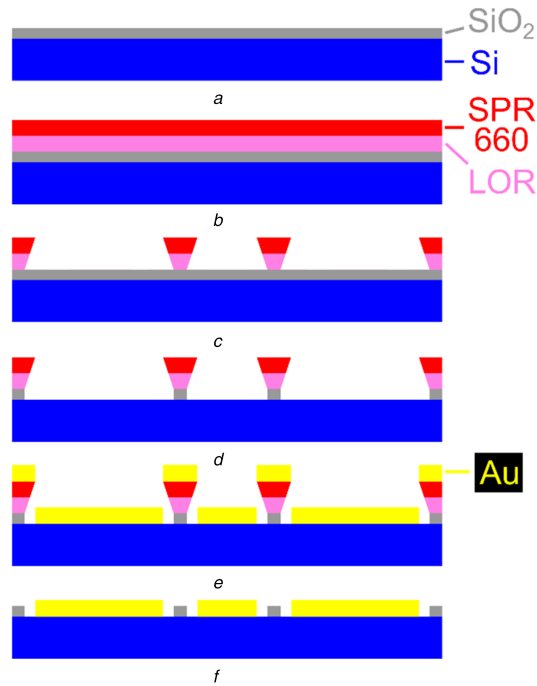


**Fig. 2** Fabrication process steps for the tunable photoconductive device (not to scale)

(a) Bare silicon substrate with native oxide layer, (b) Spin coat lift-off resist and photoresist (SPR 660), (c) Expose resist with photolithography and develop, (d) Remove native oxide with inductively coupled plasma etch with fluorine chemistry, (e) Electron-beam evaporate 500 nm gold, (f) Lift off

state  $S$ -parameter calibration artefact, since a wide variety of well-known states are necessary to estimate the values of the free parameters in the calibration model [11]. We found that the variation in the  $S$ -parameters was not monotonic with applied laser power. For example, the transmitted power in the dark state was low, rose to a maximum at the lowest measured laser power, then decreased again at the highest laser power. Qualitatively, this variation in the  $S$ -parameters comes from variation in the impedance of the MSM junctions in the device as the laser power is increased. The applied light induces photoexcited carriers in the semiconducting region and locally changes the conductivity of the silicon. This conductivity, distributed over the length of the gap in the CPW centre conductor, results in a resistance and reactance, and thus a complex total impedance, that depends on the applied laser power. As the  $S$ -parameters are a measure of the power reflected and transmitted through this gap and the complex impedance in this region directly affects how much power will be transmitted, the variation in the  $S$ -parameters is attributed to varying the applied number of photons, which is proportional to the laser power.

In order to develop a physical understanding of how the variation in these junction impedances interplay with the  $S$ -parameters, we modelled the device as a Pi network. The Pi network (Fig. 5a) included a series impedance ( $Z_3$ ) between the centre conductors and shunt impedances ( $Z_1$  and  $Z_2$ ) from the centre conductor to ground on each side of the device. We extracted the impedances in the Pi-network model by converting the error-corrected  $S$ -matrix into a  $Y$ -matrix and solving for the network admittances:  $Y_1$ ,  $Y_2$ , and  $Y_3$  at each frequency [20]. We then took the inverse of the admittance to calculate the network impedances  $Z_1$ ,  $Z_2$ , and  $Z_3$ . We found that  $Z_1$  was approximately equal to  $Z_2$  (not shown), as expected for a symmetric device. The extracted impedances and associated fits are shown in Figs. 6a and b for  $|Z_1|$  and  $|Z_3|$ , respectively. We note that the distance between the ends of the centre conductor was twice as long as the distance from the centre conductor to the ground plane; thus we expect the magnitude of  $Z_3$  to be greater than the magnitude of  $Z_1$  and  $Z_2$ . We found that the impedance of each of the elements in the Pi-network decreased monotonically with increasing laser power, consistent with the DC I-V measurements. In this work, we have focused on

particularly high laser powers in order to test the limits of the range of impedances. However, given the monotonic behaviour of the impedances with laser power, we expect that any impedance between the dark state and the highest laser-power state would be accessible by selecting an appropriate laser power.

We developed an empirical circuit model that captures the general behaviour of these impedances. The circuit model is shown in Fig. 5b and the fit parameters as a function of laser power are shown in Figs. 6c and d. The extracted impedances for  $Z_1$  and  $Z_3$  have qualitatively similar shapes, but different overall scales due to the different lengths of the conduction paths. The fit parameters of the two impedances also show similar trends. Inspired by the MSM model for the DC I-V curves, the circuit model for the device was formed from two Schottky barriers in series with a frequency-dependent impedance. The empirical model was necessary to account for the complicated photo-induced carrier dynamics in this system. We used a model with the fewest number of parameters that still produced qualitatively good fits to the data, though other models with more parameters could work as well. We used the fewest number of parameters so that we would avoid overfitting and overcomplicating the model. For the purposes of fitting  $Z_1$ , we took  $R_1 = 52 \Omega$ ,  $C_1 = 75 \text{ pF}$ ,  $C_2 = 31 \text{ pF}$ , and  $X_4 = 47 \times 10^{-35} \Omega \text{ Hz}^{-3}$  to be exact values, lumping all the fit uncertainty into the parameters that were allowed to vary with laser power ( $R_2$ ,  $C_3$ ,  $X_1$ ,  $X_2$ , and  $X_3$ ). For the purposes of fitting  $Z_3$ , we took  $R_1 = 1027 \Omega$ ,  $C_1 = 5 \text{ pF}$ ,  $C_2 = 2.5 \text{ pF}$ , and  $X_4 = 1042 \times 10^{-35} \Omega \text{ Hz}^{-3}$  to be exact, again lumping all the fit uncertainty into the parameters that were allowed to vary.

Building on the insights learned in this investigation, future work will focus on expanding the frequency range of the model, developing physical models that connect the I-V curves to the network impedances, and identifying the ideal states for operating the device as a multi-state-microwave-calibration standard. In addition to higher frequency measurements and improved models, the design of this device highlights several potential advancements. First, confining the photocarriers to a smaller region or adding an antireflective coating will allow for the use of lower laser intensities and result in a broader range of impedance states [21]. Second, the device currently gets very hot under intense laser illumination (more than 500 mW of optical power), ultimately

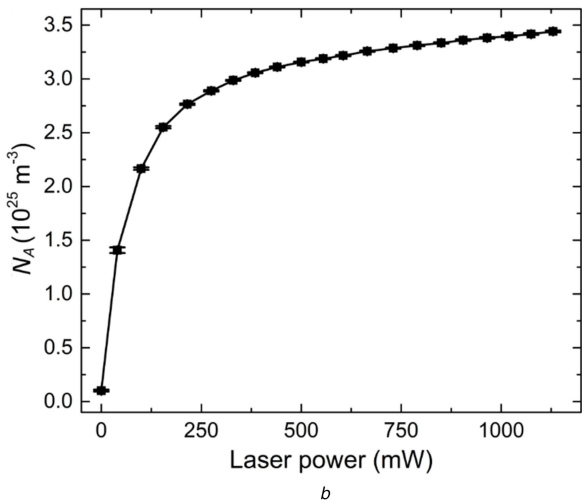
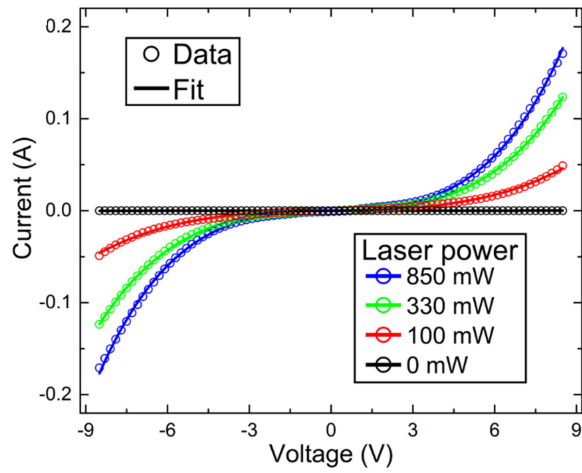


**Fig. 3** Current-voltage characteristics

(a) Select I–V curves (open circles) and associated fits (solid lines) for varying laser power, (b)  $N_A$  fit values (squares) vs. laser power from the optical probe. Error bars represent the 95% confidence interval on the fit value. Solid line in (b) is a guide for the eye. The uncertainty of the measured laser power was smaller than the data point markers. The laser was a 980 nm diode laser

causing device failure. The required optical power (and corresponding heating) could be reduced by adding an anti-reflective coating, employing a smaller active photoconductive area, or changing to a different photoconductive material. However, even without these improvements, the wide range of available impedance states and the establishment of an empirical model make photoconductors a promising candidate for multi-state-calibration devices. Currently, the effect of temperature in our device is not well understood and future work will involve including temperature dependence into our models. The DC I–V data (Fig. 3) were fit very well with a constant temperature parameter, though we do see the photocarrier density saturate at higher laser powers, which could be due to thermal effects including increased carrier–carrier scattering. Refining the frequency-dependent model using first-principles calculations to include temperature is also the target of future efforts.

#### 4 Conclusions

We proposed and demonstrated a device with an optically controlled tunable impedance over two decades in frequency (100 MHz to 40 GHz). The available range of optically controlled impedances spanned from above 10 k $\Omega$  to below 10  $\Omega$  at 10 GHz. The DC characteristics of the device were consistent with a known model for MSM junctions and the microwave-frequency behavior was well described by a newly developed empirical model. The

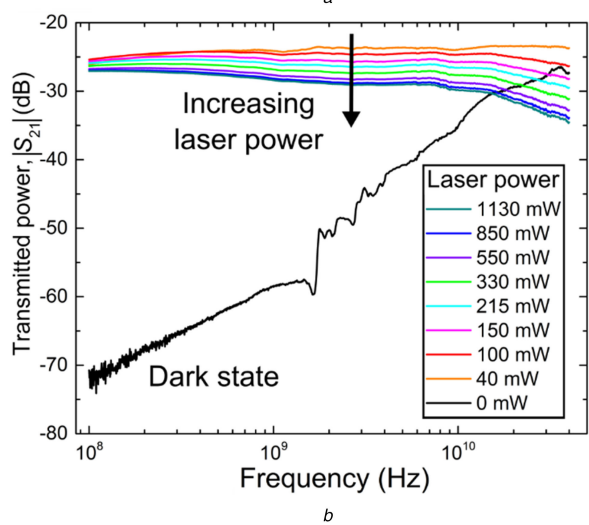
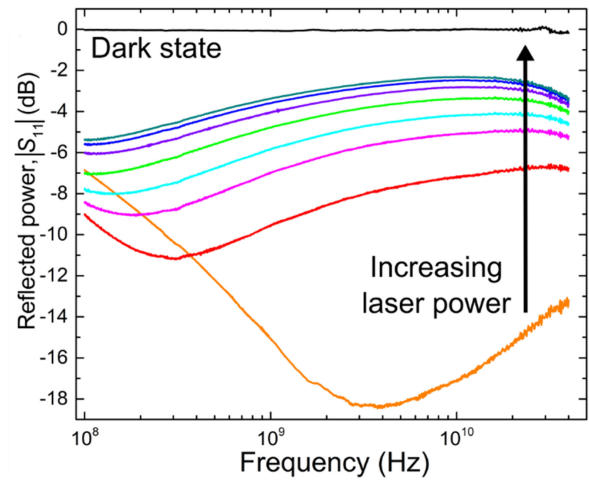


**Fig. 4** Scattering parameters

(a) Reflected power ( $S_{11}$ ) as a function of frequency for varying laser power, (b) Transmitted power ( $S_{21}$ ) as a function of frequency. The laser was a 980 nm diode laser

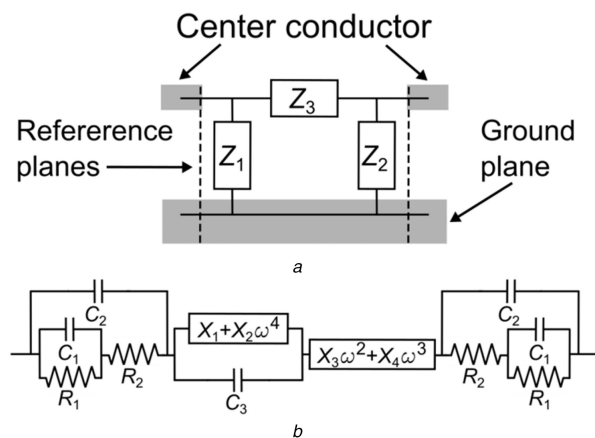


**Fig. 5** Circuit models

(a) Pi-network model, (b) Circuit model with fit parameters labelled

demonstrated range of available impedance states make optically controlled impedance devices an attractive candidate for a variety of applications, including active matching circuits, on-chip load-pull, and multi-state calibrations.

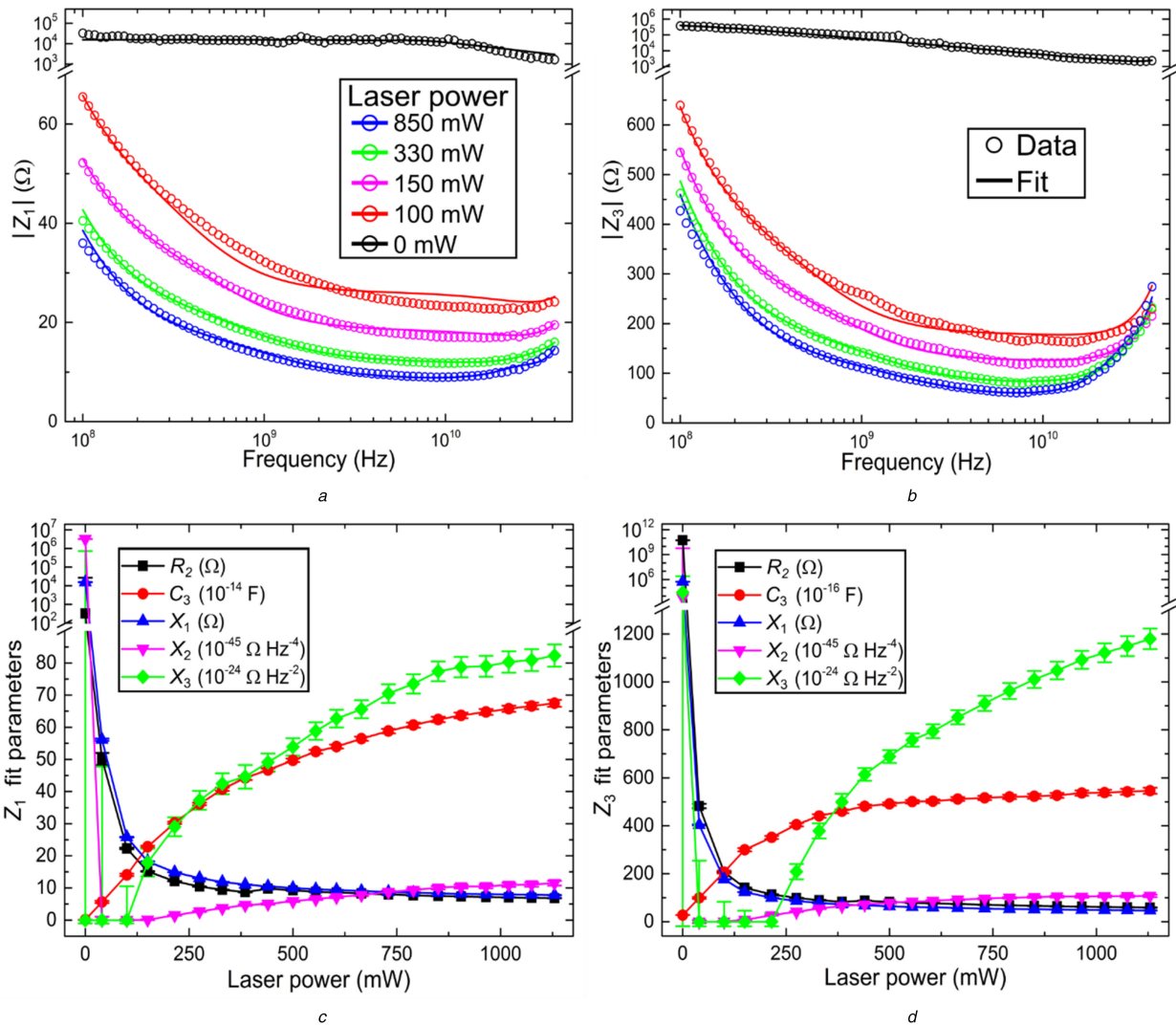


**Fig. 6** Tunable impedance and fit parameters

(a) Magnitude of measured  $Z_1$  impedances for select laser powers (open circles) and associated circuit fits (solid lines), (b) Magnitude of measured  $Z_3$  impedances for select laser powers (open circles) and associated circuit fits (solid lines). Laser power legend is the same as in (a), (c)  $Z_1$  fit parameters vs. laser power, (d)  $Z_3$  fit parameters vs. laser power. For parts (c) and (d), the solid lines are guides for the eye and error bars represent the 95% confidence interval on the fit value

## 5 Acknowledgments

This paper is an official contribution of NIST; not subject to copyright in the US. Usage of commercial products herein is for information only; it does not imply recommendation or endorsement by NIST.

## 6 References

- [1] Johnson, A., Auston, D.: ‘Microwave switching by picosecond photoconductivity’, *IEEE J. Quantum Electron.*, 1975, **11**, (6), pp. 283–287
- [2] Andersson, I.L., Eng, S.T.: ‘Phase and amplitude characteristics of InP:Fe modified interdigitated gap photoconductive microwave switches’, *IEEE Trans. Microw. Theory Techn.*, 1989, **37**, (4), pp. 729–733
- [3] Berry, C.W., Jarrahi, M.: ‘Principles of impedance matching in photoconductive antennas’, *J. Infrared, Millim., Terahertz Waves*, 2012, **33**, (12), pp. 1182–1189
- [4] Lin, I.S., McKinney, J.D., Weiner, A.M.: ‘Photonic synthesis of broadband microwave arbitrary waveforms applicable to ultra-wideband communication’, *IEEE Microw. Compon. Lett.*, 2005, **15**, (4), pp. 226–228
- [5] Kato, K.: ‘Ultrawide-band/high-frequency photodetectors’, *IEEE Trans. Microw. Theory Techn.*, 1999, **47**, (7), pp. 1265–1281
- [6] Zang, J., Morgan, J.S., Xie, X., *et al.*: ‘InP/InGaAs photovaractor’, *J. Light. Technol.*, 2018, **36**, (9), pp. 1661–1665
- [7] Verghese, S., McIntosh, K.A., Calawa, S., *et al.*: ‘Generation and detection of coherent terahertz waves using two photomixers’, *Appl. Phys. Lett.*, 1998, **73**, (26), pp. 3824–3826
- [8] Tang, Z., Pan, S.: ‘A filter-free photonic microwave single sideband mixer’, *IEEE Microw. Wirel. Compon. Lett.*, 2016, **26**, (1), pp. 67–69

- [9] Seeds, A.J.: ‘Microwave photonics’, *IEEE Trans. Microw. Theory Techn.*, 2002, **50**, (3), pp. 877–887
- [10] Ospald, F., Maryenko, D., von Klitzing, K., *et al.*: ‘1.55  $\mu\text{m}$  ultrafast photoconductive switches based on ErAs:InGaAs’, *Appl. Phys. Lett.*, 2008, **92**, (13), p. 131117
- [11] Ma, X., Orloff, N.D., Little, C.A.E., *et al.*: ‘A multistate single-connection calibration for microwave microfluidics’, *IEEE Trans. Microw. Theory Techn.*, 2017, **66**, (2), pp. 1–9
- [12] Bludau, W., Onton, A., Heinke, W., *et al.*: ‘Temperature dependence of the band gap of silicon’, *J. Appl. Phys.*, 1974, **45**, (4), pp. 1846–1848
- [13] Takeda, Y., Sasaki, A., Imamura, Y., *et al.*: ‘Electron mobility and energy gap of In $_0.53$ Ga $_0.47$ As on InP substrate’, *J. Appl. Phys.*, 1976, **47**, (12), pp. 5405–5408
- [14] Marks, R.B.: ‘A multiline method of network analyzer calibration’, *IEEE Trans. Microw. Theory Techn.*, 1991, **39**, (7), pp. 1205–1215
- [15] Williams, D.F., Wang, J.C.M., Arz, U.: ‘An optimal vector-network-analyzer calibration algorithm’, *IEEE Trans. Microw. Theory Techn.*, 2003, **51**, (12), pp. 2391–2401
- [16] Marks, R.B., Williams, D.F.: ‘Characteristic impedance determination using propagation constant measurement’, *IEEE Microw. Guid. Wave Lett.*, 1991, **1**, (6), pp. 141–143
- [17] Elhadidy, H., Sikula, J., Franc, J.: ‘Symmetrical current–voltage characteristic of a metal–semiconductor–metal structure of Schottky contacts and parameter retrieval of a CdFe structure’, *Semicond. Sci. Technol.*, 2012, **27**, (1), p. 015006
- [18] Zhang, Z.Y., Jin, C.H., Liang, X.L., *et al.*: ‘Current–voltage characteristics and parameter retrieval of semiconducting nanowires’, *Appl. Phys. Lett.*, 2006, **88**, (7), p. 073102
- [19] Chung, S.-W., Yu, J.-Y., Heath, J.R.: ‘Silicon nanowire devices’, *Appl. Phys. Lett.*, 2000, **76**, (15), pp. 2068–2070

[20] Pozar, D.: '*Microwave Engineering*' (John Wiley & Sons, Inc., USA, 2005, 4th edn.)

[21] Lee, S., Kuga, Y., Mullen, R.A.: 'Experimental results for a CW-mode optically controlled microwave switch on a silicon-based coplanar waveguide', *Microw. Opt. Technol. Lett.*, 2003, **36**, (4), pp. 257–262